PCCP

Accepted Manuscript

ROYAL SOCIETY OF CHEMISTRY

www.rsc.org/pccp

Coupled optical absorption, charge carrier separation, and surface electrochemistry in surface disordered/hydrogenated TiO_2 for enhanced PEC water splitting reaction

Dilip Kumar Behara[1], Ashok Kumar Ummireddi[1], Vidyasagar Aragonda[1], Prashant Kumar Gupta[1], Raj Ganesh S Pala[1#*] and Sri Sivakumar[1#†*]

[1]*Department of Chemical Engineering, Indian Institute of Technology Kanpur, Kanpur, UP-208016, India*

[#]*Material Science Programme, Indian Institute of Technology Kanpur, UP-208016, India*

[†]*Centre for Environmental Science & Engineering, Thematic Unit of Excellence on Soft Nanofabrication, Indian Institute of Technology Kanpur, Kanpur, UP-208016, India*

[*]Corresponding Authors: *rpala@iitk.ac.in*, *srisiva@iitk.ac.in*

Abstract

The central governing factors that influence the efficiency of photoelectrochemical (PEC) water splitting reaction are photon absorption, effective charge-carrier separation and surface electrochemistry. Attempts to improve one of three factors may debilitate other factors and we explore such issues in hydrogenated TiO_2, wherein significant increase in optical absorption has not resulted in significant increase in PEC performance which we attribute to enhanced recombination rate due to formation of amorphization/disorderness in the bulk during the hydrogenation process. To this end, we report a methodology to increase the charge-carrier separation with enhanced optical absorption of hydrogenated TiO_2. Current methodology involves hydrogenation of non-metal (N and S) doped TiO_2 which comprises (1) lowering of band gap through shifting of valence band via less electronegative non-metal N, S-doping, (2) lowering of conduction band level and band gap via formation of Ti^{3+} state and oxygen vacancy by hydrogenation, and (3) material processing to obtain disordered surface structure which favors higher electrocatalytic (EC) activity. This design strategy yields enhanced PEC activity (%ABPE=0.38) for N-S co-doped TiO_2 sample hydrogenated at 800 ºC for 24 h over possible combinations of N-S co-doped TiO_2 samples hydrogenated at 500 ºC/24 h, 650 ºC/24 h and 800 ºC/72 h. This suggests that, hydrogenation at lower temperatures does not result much increase in the optical absorption and prolonged hydrogenation results increase in the optical absorption but decrease in charge carrier separation by forming disorderness/oxygen vacancies in the bulk. Further, the difference in double layer capacitance (C_{dl}) calculated from EIS measurements of these samples reflects the change in electrochemical surface area (ECSA) and facilitates assessing the key role of surface electrochemistry in PEC water splitting reaction. Additionally, we observed blue-shift of absorption spectrum and decrease in both electrochemical (EC) and photoelectrochemical (PEC) activity after removal of surface layers through focused ion beam sputtering suggesting the importance of surface defects and photon absorption.

Keywords: Hydrogenated TiO_2, PEC water splitting, N-S co-doping, disordered shell, optical absorption, charge carrier separation, surface electrochemistry, and oxygen vacancy

1. Introduction

Recently, black hydrogenated titania was reported to enhance photocatalytic performance by creating surface disorderness that helps in improving visible light absorption[1]. Further, the surface defects (oxygen vacancies/Ti^{3+} states) created upon amorphization will enhance the electrical conductivity which is essential for wide band gap materials like TiO_2[1-8]. Therefore, stabilization of surface defects is essential for better utilization of TiO_2 material for photocatalytic applications in long run. However, the stabilization of these defects is challenging and control of these oxygen vacancies is highly difficult as they depend on parameters such as temperature, surface states and synthesis conditions. Recently, Lin *et al.* made an attempt in better utilization of surface defects by addition of dopants to the surface disordered TiO_2 material[4]. They have synthesized oxygen deficient TiO_{2-x} by hydrogenation followed by post doping of non-metal (H, N, and I) and observed enhanced acitivity in photocatalytic H_2 generation which is attributed to reduction in surface defects due to doping. Formation of surface defects can be further controlled by predoping of non-metal during the synthesis of TiO_2 followed by controlled hydrogenation. In the proposed methodology, we have done non-metal (N and S) doping followed by hydrogenation. Since the dopants (N and S) chosen in this methodology are less electro-negative in comparison to oxygen, lesser is the energy required for hydrogen to remove these dopants (than oxygen) and create/stabilize the anion vacancies. We optimized the hydrogenation temperature and time (800 ^{O}C and 24 h) such that hydrogen diffuses on the surface but not to the bulk (lesser the hydrogenation temperature and time results in hydrogenating the surface and more the hydrogenation temperature and time results in hydrogenating to the bulk). In this methodology, anion vacancies are predominantly present on the surface rather than in bulk which reduce the charge carrier recombination and the element doped in the bulk increases the absoprtion cross-section.

To this end, we report the synthesis of N-S co-doped TiO_2 followed by hydrogenation for enhanced PEC water splitting. In these doped hydrogenated TiO_2 nanostructures, interaction of trapped electrons in oxygen vacancies (V_o) present on the surface and adjacent Ti^{4+} centers lead to formation of Ti^{3+} states. These electronic levels form below the conduction band and contribute to enhance optical

absorption cross-section[9]. Further, the electro/photoelectrocatalytic properties of these doped hydrogenated TiO_2 nanostructures will be improved due to following reasons: 1) presence of under co-ordinated or strained bonds on surface helps in increasing electrocatalytic properties[10-13]; 2) synergestic effect between added dopant and hydrogen treated to the system will stabilize the oxygen vacancies and improve the performance[14-18].

In this work, we report 1) multi-element (N-S) doped hydrogenated TiO_2 nanostructures fabricated on stainless steel (SS) substrate via "click" chemistry for enhanced PEC water splitting reaction, and 2) role of surface defects (oxygen vacancies/Ti^{3+} states) in amorphous layer of hydrogenated TiO_2 material in charge-carrier transport. Nitrogen and sulphur are chosen as dopants as they are less electronegative than oxygen and expected to reduce the band-gap by introducing electronic states above valence band (VB) levels of TiO_2 upon substitutional doping. Further, hydrogenation will lead to stabilization of Ti^{3+} states which is expected to lower band gap through lowering of conduction band and also helping in achieving amorphization of surface layer which will lead to increased electrocatalytic property. From EC/PEC measurements, it is observed that doped hydrogenated TiO_2 nanostructures perform better than unhydrogenated undoped/doped and hydrogenated undoped TiO_2 nanostructures underlying the importance of combined effect of doping and hydrogenation. The calculated efficiency metrics of hydrogenated N-S co-doped TiO_2@800ºC/24h sample yields an applied bias photon to current conversion efficiency (ABPE) of 0.38%@0.63 V applied bias, intrinsic solar to chemical conversion (ISTC) efficiency of 0.031 (or 3.1%)@1.27 V vs. RHE (reversible hydrogen electrode) and electrical and solar power-to-hydrogen conversion (ESPH) efficiency of 6.6%@1.56 V applied bias respectively which is higher than undoped/doped TiO_2 nanostructures hydrogenated at different temperature and time periods. The enhancement in PEC performance in doped hydrogenated TiO_2 is attributed to the combined effect of doping, oxygen vacancy states and Ti^{3+} states. We note that, 24 h hydrogenated sample possess higher bandgap (~ 2.95 eV), but shows enhanced efficiency in comparison to 72 h hydrogenated sample (~ 2.94 eV). Though, there is no significant difference in optical bandgap measured from tauc plots of 24 h and 72 h hydrogenated samples, there is noticeable difference in double layer capacitance (Table S6b) is

observed. This suggests changes in electrochemical surface area (ECSA) available for electrochemical reaction, which signifies the prominent role of surface electrochemistry in PEC water splitting reaction. Further, the interfacial kinetics of surface disordered TiO_2 nanostructures calculated from electrochemical impedance spectroscopy (EIS) studies under light illumination also support optical absorption and charge carrier separation are not mutually exclusive path ways in enhancing the PEC performance of surface disordered/hydrogenated TiO_2 and it is not enough to just increase optical absorption while trying to increase the PEC efficiency, but increase of PEC efficiency requires a finer balance of optimizing optical absorption without severely debilitating electron-hole separation. The role of disordered surface generated due to hydrogenation in enhancing PEC activity is demonstrated by removal of few surface atomic layers from doped hydrogenated TiO_2 nanostructure by focused ion beam (FIB) sputtering upon which a decrease in both EC/PEC activity and photon absorption cross-section in comparison to un-sputtered sample is observed. This result gives credence to the need of disordered surfaces in TiO_2 for obtaining enhanced PEC performance.

2. Experimental section

2.1 Synthesis of undoped and doped TiO_2 nanoparticles

Titanium (IV) iso-propoxide (TTIP, 9 ml) was added drop wise into a homogeneous mixture of ethanol (150 ml) and water (9.75 ml). The reaction mixture was kept at 85 °C for 4 h under agitation followed by evaporation of ethanol. The sample was dried at 60 °C for 30 min to get TiO_2 nanopowder which was finely grounded and calcined at 400 °C for 3 h to yield anatase TiO_2 phase[21]. For synthesis of doped TiO_2 nanoparticles, different precursor salts/solutions were used for different dopants. Nitrogen doping was achieved by addition of 5 ml aq. NH_3 solution. Similarly, a solution of 9.3 g thio-urea in 3.75 ml DI water was used as precursor for sulphur doping. For N-S co-doped TiO_2 nanoparticle synthesis, a mixture of 2.5 ml aq. NH_3 and 5.4 g thio-urea was used as precursor solution. Above mentioned undoped TiO_2 experimental protocol was followed except the addition of respective precursor salt/solution before TTIP to ethanol-water mixture.

2.2 Hydrogenation of undoped/doped TiO_2 nanoparticles

Calcined samples (undoped and doped TiO_2 nanoparticles) were pelletized and hydrogenated at different temperatures in a range of 500 °C to 800 °C for 24 h and 72 h at 20 bar pressure in hydrogenation chamber. The digital photograph of the reactor was used for hydrogenation process is shown in Figure S1a. It is also important to eliminate the possibility of "blackness" in TiO_2 due to carbon intercalation, which is not easy to remove because of presence of reducing hydrogenation condition. In the present studies, the possibility of carbon induced blackness was eliminated by careful XPS studies. We note that reaction conditions have to be maintained precisely to reproduce the results.

2.3 Fabrication of nanostructured TiO_2 electrodes

Scheme 1 shows schematic representation for the synthesis of hydrogenated N-S co-doped TiO_2 nanostructures followed by clicking onto alkyne functionalized stainless steel (SS) substrate using click chemistry. It involves four steps: 1) synthesis of doped TiO_2 nanostructures; 2) hydrogenation of doped TiO_2 nanostructures at various temperatures (500 ºC, 650 ºC, and 800 ºC) and time periods (24 h, and 72 h); 3) surface functionalization of TiO_2 nanostructures with azide group (section 1.2, S.I); 4) surface functionalization of SS substrate with alkyne group (section 1.3, S.I) respectively; and 5) coating of TiO_2 nanostructures onto SS substrates via click chemistry (section 1.4, S.I).

3. Results and Discussion

3.1 Material Characterization

3.1.1 XRD analysis

XRD data of hydrogenated doped TiO_2 nanostructures prepared at various temperatures and for different time durations are shown in Figure 1a and Figure S2. XRD data of samples hydrogenated at 500 °C for 24 h (i.e. hydrogenated anatase TiO_2@500ºC/24h, hydrogenated N doped TiO_2@500ºC/24h, hydrogenated S doped TiO_2@500ºC/24h, and hydrogenated N-S co-doped TiO_2@500ºC/24h) confirms presence of anatase phase with JCPDS card no: 00-004-0477 (Figure 1 and Figure S2b). Up to the hydrogenation temperature of 650 °C, there is no appearance of rutile phase as evident from hydrogenated N-S co-doped TiO_2@650ºC/24h sample which shows pure anatase phase (Figure 1a). Further increase of

hydrogenation temperature leads to formation of rutile as major phase along with small amount of anatase phase in hydrogenated N doped TiO_2@700ºC/24h (Figure S2b and S2c**)**, hydrogenated N-S co-doped TiO_2@800ºC/24h, and hydrogenated N-S co-doped TiO_2@800ºC/72h samples respectively (Figure 1). The formation of mixed phase is further supported from HRTEM/SAED analysis (Figure 3 and 4). The N doped, S doped and N-S co-doped TiO_2 nanostructures calcined at 400 ºC possess crystallite sizes of ~ 11.5 nm, 7.8 nm, and 4.2 nm respectively which are lesser than undoped TiO_2 (~ 17.7 nm) (Figure S2a). The decrease in the crystallite size of single element (N or S) and multi element (N-S co-doped) TiO_2 sample compared to un-doped TiO_2 suggests the dopant incorporation in crystalline matrix[19, 20]. Further, broadening of diffraction peaks of doped (N or S or N-S) TiO_2 nanostructures in comparison with un-doped TiO_2 nanostructures supports the modification of crystalline lattice parameters upon doping.

3.1.2 Electron microscopy studies

To study the morphology and subsequent changes in undoped/doped TiO_2 nanostructures during hydrogenation step, scanning electron microscopy (SEM) images were taken (Figure 2, S3, and S4). N-S co-doped TiO_2 sample hydrogenated at 500 ºC temperature for 24 h shows irregular morphology with increased aggregation as compared to unhydrogenated sample (Figure 2a). Further, same sample hydrogenated at elevated temperatures (650 °C and 800 °C) for 24 h/72 h shows larger clusters with irregular morphology (Figure 2b, 2c and 2d). Therefore, it can be concluded that the surface morphology of multi-element doped TiO_2 nanostructures enormously changes with increase in hydrogenation temperature. The amorphous TiO_2 (uncalcined) and crystalline TiO_2 (calcined) nanoparticles show spherical morphology with size range from 110-160 nm (Figure S3a, S3b). N doped and S doped TiO_2 nanoparticles also possess spherical shape with particle size of ~100±10 nm and 175±10 nm, respectively (Figure S3c, S3d). However, co-doping with nitrogen and sulphur to TiO_2 leads to anisotropical morphology (Figure S3e). Moreover, undoped/single element doped (N or S) TiO_2 samples hydrogenated at 500 °C for 24 h lead to increase in particle size compared to unhydrogenated samples, while retaining spherical morphology (Figure S4). Additionally, SEM image of N doped TiO_2 clicked over SS substrate (Figure S4d) shows good surface coverage. Further, EDAX analysis (Figure S3f, and Table S1) confirms

the presence of Ti and O elements along with dopants nitrogen (N) and sulphur (S). We believe that the photo efficiency can be further enhanced by the precise optimization of dopant and hydrogenation conditions.

The morphology, crystallinity and formation of amorphous layer upon hydrogenation have been further confirmed from transmission electron microscopy (TEM), high resolution transmission electron microscopy (HRTEM) and selective area electron diffraction (SAED) studies (Figure 3, 4, and S5). TEM images of hydrogenated N-S co-doped TiO_2@500ºC/24h (Figure 3a) and N-S co-doped TiO_2@650ºC/24h (Figure 3c) show the particles with irregular morphology and the indexed SAED pattern (Figure 3b, 3d) confirms the presence of anatase phase which matches with XRD data (Figure S2d). Further, N-S co-doped TiO_2 samples hydrogenated at 800 °C for 24 h and 72 h also show irregular morphology (Figure 3e, 3g) but possess both anatase and rutile crystalline phases. This is further supported by indexed SAED pattern (Figure 3f and 3h) and XRD data (Figure 1a). Figure 4 shows the HRTEM information of N doped TiO_2 hydrogenated at 700 °C for 24 h. The contrast in the TEM image clearly demarcates the rutile and anatase phases with lattice fringes (Figure 4a). Further, HRTEM image (Figure 4b) confirms the formation of disordered/amorphous layer over crystalline core with thickness ~ 0.5 nm, which indicates that hydrogenation has created the surface defects (Figure 4b) in TiO_2 material. The calculated d-spacing values of 0.1462, 0.2313 and 0.2145 nm corresponds to anatase phase and (130), (200), (111) planes correspond to rutile phases respectively (Figure 4b). Further, Figure S5 shows the TEM images and SAED pattern of crystalline TiO_2 and N doped TiO_2 hydrogenated for 500 ºC for 24 h. TEM images (Figure S5a and S5c) of both samples show particles with irregular shape and SAED indexed patterns (Figure S5b and S5d) shows pure anatase phase.

3.1.3 Raman spectra analysis

Raman spectra of undoped, doped and hydrogenated doped samples are shown in Figure 1b and S6. Raman spectra of unhydrogenated undoped/doped samples (Figure S6a) depict four major intense peaks observed at 143 cm^{-1}, 395 cm^{-1}, 513 cm^{-1} and 639 cm^{-1}, attributed to E_g band, B_{1g} band, A_{1g}+B_{1g} and E_g bands of anatase phase of TiO_2 respectively. Further, hydrogenated TiO_2@500ºC/24h, hydrogenated N

doped TiO_2@500ºC/24h, hydrogenated S doped TiO_2@500ºC/24h, hydrogenated N-S co-doped TiO_2@500ºC/24h and hydrogenated N-S co-doped TiO_2@650ºC/24h possess anatase bands (Figure S6b and 1b**)** which confirms the anatase crystalline phase consistent with XRD data (Figure S2b). However, N-S co-doped TiO_2@800ºC/24h and N-S co-doped TiO_2@800ºC/72h samples show three peaks located at ~234 cm^{-1}, 443 cm^{-1} and 610 cm^{-1}, attributed to B_{1g}, E_g, and A_{1g} bands of rutile TiO_2 phase respectively, which is consistent with its XRD data (Figure 1a). Further, N doped TiO_2@700ºC/24h possess both anatase and rutile bands indicating both anatase and rutile crystalline phases formation, which is consistent with its XRD data (Figure S2b). Additionally, a small shift along with broadening of peak is observed at 141 cm^{-1}(E_g), (attributed to both anatase and rutile phases) with N doped hydrogenated TiO_2@500ºC/24h and N doped TiO_2@700ºC/24h nanostructures in comparison to N doped TiO_2 nanostructure (Figure S6c). Further, the same observation is found for hydrogenated N-S co-doped TiO_2@650ºC/24h sample (B_{1g}) as shown in Figure S6d. The shift and broadening of the peak indicate the non-stoichiometry or reduction in original symmetry of TiO_2 lattice due to surface disorder[21]. Additionally, Raman spectra of hydrogenated TiO_2@500ºC/24h sample, shows two peaks at 1339 cm^{-1} (D band) and 1606 cm^{-1} (G band), which are attributed to Ti-H vibrations or surface disorder defects created due to the presence of carbon, wherein D and G bands (which are due to presence of carbon in SS substrate) will also emerge at the same wavenumbers (Figure S18a).

3.1.4 FTIR analysis

FTIR spectra of undoped/doped/hydrogenated TiO_2 nanostructures are shown in Figure S7, S8, and Table S2. FTIR spectra (Figure S8b) of hydrogenated TiO_2 nanostructures show reduction in –OH peak intensity in comparison to unhydrogenated nanostructures suggests that the reduction of -OH groups present in TiO_2 sample. The presence of dopants N, S in TiO_2 matrix is confirmed from Ti-S and Ti-N characteristic peaks as shown in Figure S7c and S7d and Table S2. Further, the peaks at ~3645, 3670 and 3685 cm^{-1} of hydrogenated S doped TiO_2@500ºC/24h sample are attributed to the tetrahedral co-ordinated vacancies (Figure S8a)[22]. FTIR spectra of azide functionalized undoped/doped and doped-hydrogenated TiO_2 particles show a peak at ~ 2110 cm^{-1} (Figure S7b) which confirms the presence of azide group on

particles. Additionally, FTIR spectra of alkyne functionalized SS substrate show a peak at ~2156 cm^{-1} confirming the presence of alkyne group (Figure S8b). All functionalized TiO_2 nanostructures show the presence of strong -CH_2 stretch at ~2950 cm^{-1} confirming the surface modification. Further, increase in contact angle (~97.50°) in the case of alkyne functionalized electrode (hydrophobic) compared to bare SS substrate/electrode (~60°) (Figure S8c), suggests the presence of terminal alkyne moiety on surface which matches with our earlier report[23].

3.1.5 UV-Vis spectra analysis

UV-Vis spectra of undoped/doped and hydrogenated doped TiO_2 samples are shown in Figure S9. The approximate band gaps of all TiO_2 nanostructures calculated from tauc plots (undoped/doped/hydrogenated doped TiO_2) are summarized in Table S3. The decrements in optical bandgap in doped and hydrogenated samples are clearly visualized with color of samples (Figure S1b-n). Both amorphous (uncalcined) and crystalline (calcined) TiO_2 samples show absorption bands around 387 nm and 392 nm (Figure S9a) which correspond to bandgap of 3.66 eV, and 3.46 eV respectively measured from corresponding tauc plots (Figure S9b). A red shift in absorption band is observed when TiO_2 matrix is doped. The measured band gap for N doped TiO_2, S doped TiO_2 and N-S co-doped TiO_2 are found to be ~ 3.38 eV, 3.37 eV, and 3.09 eV respectively. S dopant due to its lower electronegativity can shift VB to more upward direction in comparison to N dopant, although both seem to possess same absorption cross-section. Further, N-doping leads to stabilization of Ti^{3+} states[14, 24]. For this reason, co-doping leads to lowering of band-gap more than individual doping (S or N). Further, absorption spectra of hydrogenated TiO_2 nanostructures (Figure S9c) show red-shift with less optical band gap compared to their unhydrogenated counter parts. This is attributed to formation of mid-gap states between CB and VB due to hydrogenation and formation of oxygen vacancy and Ti^{3+} states.

3.1.6 Electron paramagnetic resonance (EPR) analysis

Ti^{3+} surface defects is quite different from oxygen vacancies (V_o)[19]. It is to be noted that Ti^{3+} states will be generally formed by reduction of Ti^{4+} in either of the two ways: 1) Ti^{4+} ion receives a photo electron usually by UV light absorption on TiO_2 surface. The electrons can be trapped and tend to reduce

Ti^{4+} cations to Ti^{3+} states[19, 20]. Similarly, oxygen vacancies (V_o) are responsible for formation of color (F) centers, as the electron pair that remains trapped in cavity (V_o), upon loss of an oxygen atom from the surface of metal oxide[25]. Electron paramagnetic resonance (EPR) spectra is used to confirm the presence of surface defects (oxygen vacancies/Ti^{3+} states) in surface disordered/hydrogenated TiO_2 sample. It is known that for paramagnetic materials containing ''F-centers'' or oxygen vacancies, the resonance at g = 2.004, is the most prominent and characteristic electron signal[26]. Undoped TiO_2 nanostructures show a g-value of ~2.003-2.004 (Figure S10a), which is attributed to the existence of oxygen vacancies. Further, N-S co-doped TiO_2 samples hydrogenated at 500 °C, 650 °C and 800 °C for 24 h, results in additional peak at g~1.996 to 1.999 along with small shift in original oxygen vacancy state (g ~ 2.003-2.007) (Figure S10b, e, f). Peak emerged at g = 1.996 to 1.999 in these samples is attributed to Ti^{3+} states due to interaction of H atoms and Ti^{4+} state of TiO_2 leading to formation of Ti^{3+} states (eq. 1).

$$O^{2-} + 2Ti^{4+} + H_2 \rightarrow 2Ti^{3+} + H_2O \quad \ldots\ldots\ldots\ldots \quad (1)$$

This observation clearly confirms the presence of oxygen vacancies and Ti^{3+} states upon hydrogenation which is consistent with earlier reports[21, 27]. Further, doped unhydrogenated TiO_2 sample (N-S co-doped TiO_2) also shows characteristic signal nearer to g value of 1.997 indicating the presence of Ti^{3+} states (Figure S10c, d). Therefore, Ti^{3+} states are present along with oxygen vacancies before hydrogenation (i.e. in doping stage) which is consistent with previous reports[28]. Although, it is highly difficult to demarcate the presence and individual role of oxygen vacancies relative to Ti^{3+} states in showing enhanced PEC performance of doped cum hydrogenated TiO_2 samples[29], we attempted to find out the relative change in concentration of oxygen vacancies from Mott-Schottky plots (Figure S11)[28, 30]. Since oxygen vacancies act as electron donors, increase in the donor density can be attributed to the increase in concentration of oxygen vacancies. The donor density can be calculated from the relation

$$N_d = \left(\frac{2}{e_0 \varepsilon \varepsilon_0}\right)\left(\frac{dC^2}{dV}\right)^{-1} \quad \ldots\ldots\ldots\ldots\ldots \quad (2)$$

where N_d is the donor density, e_0 is the electron charge, C is the capacitance, ε is the dielectric constant of TiO_2 (~31 in case of anatase TiO_2)[31], ε_0 is the permittivity of vacuum, and V is the potential applied at the

electrode. The calculated slopes from Mott-Schottky plots, for anatase TiO_2, hydrogenated N-S co-doped TiO_2@800°C/24h, and hydrogenated N-S co-doped TiO_2@800°C/72h are found to be 6.87 x 10^{10} $cm^4F^{-2}V^{-1}$, 4.44 x 10^{10} $cm^4F^{-2}V^{-1}$, and 4.34 x 10^{10} $cm^4F^{-2}V^{-1}$ respectively. Further, the donor densities of the anatase TiO_2, hydrogenated N-S co-doped TiO_2@800°C/24h, and hydrogenated N-S co-doped TiO_2@800°C/72h are calculated to be 0.66 x 10^{20}, 1.02 x 10^{20} and 1.05 x 10^{20} cm^{-3} respectively. Increase in the donor density of hydrogenated N-S co-doped TiO_2@800°C/72h, hydrogenated N-S co-doped TiO_2@800°C/72h samples with respect to anatase TiO_2, suggests that there is an increment in the concentration of oxygen vacancies in doped hydrogenated samples (hydrogenated N-S co-doped TiO_2@800°C/72h, and hydrogenated N-S co-doped TiO_2@800°C/24h) over undoped unhydrogenated sample (anatase TiO_2).

3.1.7 X-ray Photoelectron Spectroscopy (XPS) analysis

X-ray photoelectron spectroscopy (XPS) reveals the presence of elements and associated chemical bonds on the surface within few atomic layers of the material. Two peaks of Ti $2p_{3/2}$ (456.8 eV) and Ti $2p_{1/2}$ (462.7 eV) are observed for hydrogenated N-S co-doped TiO_2@650°C/24h nanostructure (Figure S12), which confirms the presence of Ti^{3+} states ($Ti^{4+} + e^- \rightarrow Ti^{3+}$). The observed binding energies of 284.05 eV, 162.5 eV, 232.6 eV, and 397.7 eV represent C 1s, S 2p, S 2s and N 1s signals respectively (Figure S12a). Further, XPS measurements were taken at slow scan rates to magnify the Ti and O peaks. Two nearby peaks are observed at binding energies ~ 55.1 eV and 61.6 eV which correspond to Ti 3s states. Additionally, O 1s peak can be resolved into two peaks at about 530.39 eV and 531.2 eV, wherein peak at 530.39 eV is attributed to Ti-O-Ti groups on surface and broader peak at 531.2 eV can be attributed to Ti-OH (Figure S12b and S12c). These observations confirm the presence of dopants as well as defect states in TiO_2 matrix. Further, deconvoluted XPS spectra for hydrogenated N-S co-doped TiO_2@800°C/24h nanostructure is shown in Fig 5. Four peaks at 557.7 eV, 558.6 eV, 559.3 eV and 564.6 eV was observed from deconvoluted XPS Ti 2p spectra. The peaks at 558.6 eV and 564.6 eV can be attributed to $2p_{3/2}$ and $2p_{1/2}$ of Ti^{4+} ion states (Figure 5c) and peaks at 557.7 eV (Figure 5d) and

559.3 eV (Figure 5c) can be attributed to $2p_{3/2}$ and $2p_{1/2}$ of Ti^{3+} states respectively, confirms the presence of Ti^{3+} states and defect states in TiO_2 matrix (Figure 5d) consistent with earlier reports[32-34].

We have performed XPS measurements to determine the valence band edge position of anatase TiO_2 and hydrogenated N-S co-doped TiO_2@800ºC/24h samples (Figure S13). The calculated valence band edge position of anatase TiO_2 is about 1.29 eV, whereas 0.86 eV in case of hydrogenated N-S co-doped TiO_2@800ºC /24h sample. This confirms the shift of valence band edge position of hydrogenated N-S co-doped TiO_2@800ºC/24h sample is by 0.43 eV towards vacuum. Since, the difference in optical bandgap between anatase TiO_2 and N-S co-doped TiO_2@800ºC/24h is about 0.51 eV, the rest of the fraction can be considered as shift in the conduction band edge towards valence band.

3.2 Electrochemical (EC)/Photoelectrochemical (PEC) water splitting

The performance of fabricated nanostructures towards photoelectrochemical (PEC) water splitting is evaluated using both two probe and three probe methods[35]. Current vs. applied bias/applied potential plots were recorded for all fabricated undoped/doped/hydrogenated doped TiO_2 nanostructured electrodes in 2-probe (Figure 6, S14, S15, and Table S4) and 3-probe modes (Table S5) in 0.1M NaOH solution (pH~13.6). The observed onset working electrode potential of fabricated nanostructured electrodes is 0.52-0.6 V vs. Ag/AgCl (1.52-1.6 V vs. RHE) corresponds to the oxygen evolution reaction (OER) potential. The best performance among all the prepared hydrogenated doped TiO_2 samples is found to be for hydrogenated N-S co-doped TiO_2@800ºC/24h sample with a current density of 6.3 mA/cm^2 (under light) and 4.7 mA/cm^2 (under dark) at 1.6 V applied bias respectively measured in 2-probe mode (Figure 6d). Further, the same electrode shows a current density of 31.4 mA/cm^2 (under light) and 25.6 mA/cm^2 (under dark) in three-probe mode at a working electrode potential of 1.2 V vs. Ag/AgCl (2.2 V vs. RHE) applied potential (Table S5). Two-probe measurements of undoped/doped/hydrogenated doped TiO_2 nanostructured electrodes are shown in Figure S14 and S15.

From Table S5, it is observed that hydrogenated TiO_2 nanostructures show enhanced PEC activity in comparison to unhydrogenated TiO_2 nanostructures. From the table, N doping in TiO_2 improves EC activity but S doping does not. This can be rationalized from the fact that aliovalent N-doping leads to

formation of Ti^{3+} state which helps in increasing EC activity. However, isovalent S-doping does not lead to formation of any intermediate Ti^{3+} state, which contributes towards improvement in EC activity. Further due to less electronegativity of S, there would be less charge polarization over Ti-atom which slightly lowers EC activity towards water splitting as evident from lower EC activity of S doped TiO_2 in comparison to TiO_2. However, co-doped TiO_2 shows higher EC activity than both monodoped N- and S-doped TiO_2 due to either synergistic interplay of both dopants in enhancing the activity and/or improved electronic conductivity[36-38]. It is also observed that all the hydrogenated samples show better EC activity in comparison to their unhydrogenated counterparts. This result implies that amporphization due to hydrogenation process improves EC activity towards water splitting. However, EC activity of the hydrogenated samples significantly depends on the hydrogenation temperature which determines the crystalline phase. Among the co-doped hydrogenated TiO_2 samples, the EC activity is found to be in order hydrogenated N-S co-doped TiO_2@800ºC/24h > hydrogenated N-S co-doped TiO_2@800ºC/72h > hydrogenated N-S co-doped TiO_2@650ºC/24h > hydrogenated N-S co-doped TiO_2@500ºC/24h. The increased EC activity of hydrogenated N-S co-doped TiO_2@800ºC/24h may be attributed to synergistic effect of rutile and small amount of anatase present in the sample. In this regard, it is pointed out that mixed phase shows better EC activity in comparison to any single phase[39, 40]. However, increase of rutile phase beyond a percentage leads to reduction in EC activity[41]. Further, the decrease in dark current of hydrogenated N-S co-doped TiO_2@800ºC/72h sample in comparison to hydrogenated N-S co-doped TiO_2@800ºC/24h sample (Table S4) may be attributed to decrease in electrochemical surface area (ECSA) upon hydrogenation for longer time (72 h), which is supported by decrease in double layer capacitance (C_{dl}) calculated from EIS circuits (Table S6b, section 3.3).

In order to compare the photo-performance of the electrodes, the applied bias photon to current conversion efficiency (ABPE) has been calculated using the following relation,

$$ABPE = \left[\frac{\left|j_{ph}(mA/cm^2)\right| \times \left((1.23 - |V_b|)(V)\right)}{P_{total}(mW/cm^2)}\right]_{AM\ 1.5G} \quad \ldots\ldots\ldots\ldots\ldots (3)$$

Where j_{ph} is photocurrent, V_b is applied bias between working and counter electrode and P_{total} is intensity of light (power) from solar simulator. Since, the photocurrent developed at low applied bias values play an important role in characterizing any photo material, we have taken the true activity of photo material by measuring applied bias to photo current conversion efficiency (ABPE), which signifies the minimum applied bias (below thermodynamic potential of water i.e. 1.23 V), at which maximum photon to current conversion is achieved[42-44]. The measured ABPE values of unhydrogenated and hydrogenated samples prepared at different temperatures and time periods are compared at 0.63 V and tabulated in Table S3. Among all the prepared electrodes, the best ABPE value is found for hydrogenated N-S co-doped TiO_2@800ºC/24h sample with a value of ~ 0.38%, at 0.63 V applied bias (Figure 6f). Therefore, the best photo activity performed sample in this work is hydrogenated N-S doped TiO_2@800ºC/24h and is chosen based on true ABPE value. We conclude from above values that hydrogenated undoped/doped TiO_2 nanostructures show better PEC performance than unhydrogenated nanostructures and we can attribute the enhanced performance to reduction in charge carrier recombination as well as improvement in optical absorption with the proposed design strategy. From Table S3, it is found that both N-doping and S-doping yields enhancement of ABPE which can be ascribed to enhancement of photon absorption cross-section. The co-doping leads to better ABPE value than any singular N- or S-doping (Figure S16). The order of ABPE among co-doped hydrogenated TiO_2 samples is found to be N-S co-doped TiO_2@800ºC/24h > hydrogenated N-S co-doped TiO_2@800ºC/72h > hydrogenated N-S co-doped TiO_2@650ºC/24h > hydrogenated N-S co-doped TiO_2@500ºC/24h. The PEC activity in the disordered mixed phase is higher in comparison to anatase phase[40, 41, 45]. It is evident from the above results that hydrogenation at higher temperature enhances the efficiency. It is to be noted that, 24 h hydrogenated sample with optical bandgap of ~2.95 eV shows enhanced efficiency in comparison to 72 h hydrogenated sample having bandgap of ~2.94 eV. The reduction in PEC performance of 72 h hydrogenated sample over 24 h hydrogenated sample can be attributed to 1) decrease in electrochemical surface area (ECSA) (Table S6b) as explained

in section 3.3, and 2) high charge carrier recombination that persists due to defect states/oxygen vacancies developed in bulk.

The PEC performance of the electrodes is also benchmarked by comparing intrinsic solar to chemical conversion (ISTC) efficiency. This efficiency is calculated using three-electrode cell potentials (Figure 7) which measures the maximum intrinsic power of photo-anode to convert the solar light into chemical energy as per below relation,

$$ISTC = \frac{\eta_F \times 1.23(V)}{V_{dark}(V)} \times \frac{\left|j_{ph}(mA/cm^2)\right| \times V_{photo}(V)}{P_{solar}(mW/cm^2)} \quad \ldots\ldots\ldots\ldots\ldots (4)$$

Where photocurrent (j_{photo}, difference of current density obtained with and without light at the same potential) is in mA/cm^2, on the other hand photo voltage i.e. V_{photo} is the difference of potentials under light (V_{light}) and dark (V_{dark}) conditions at same current density. Further, maximum internal photovoltaic power of TiO_2 nanostructures is calculated from the plot between j_{photo} and V_{photo} as shown in Figure 7b. For instance, under light illumination hydrogenated N-S co-doped TiO_2@800ºC/24h shows the photocurrent of ~ 0.58 mA/cm^2 at 1.45 V (vs. RHE) whereas to obtain same current under dark condition, this sample requires 1.48 V (vs. RHE) which means solar light provides energy corresponds to potential of 0.036 V or power of ~0.021 mW/cm^2. As mentioned by Grätzel and co-workers, external power is saved as a result of the internal photovoltaic power of this sample which is calculated by the reduction in the water electrolysis conversion efficiency i.e. 1.23 (V_{RHE})/$V_{dark,\ RHE}$ = ~ 82%. Thus, ISTC efficiency of this sample is ~ 0.82 × 0.021 = 0.0172 or 1.72% (Figure 7a). The maximum ISTC efficiency of ~ 3.1% is obtained for hydrogenated N-S co-doped TiO_2@800ºC/24h compared to other hydrogenated samples. Significance of ISTC can be further understood as follows; maximum current density obtained at 1.45 V (vs. RHE) with hydrogenated N-S co-doped TiO_2@800ºC/24h is 0.775 mA/cm^2 which means that this electrode can produce the maximum chemical power of ~0.953 mW/cm^2 and in this total power output, internal solar conversion to chemical power of hydrogenated N-S co-doped TiO_2@800ºC/24h contributes ~ 0.0172 i.e.1.8% and remaining power could be supplied from external electrical energy. ISTC provides

only half cell efficiency (as it is measured in three electrode configuration) and does not include losses from other components of PEC cell i.e. counter electrode, electrolyte, wires etc. Further, both the efficiencies i.e. ABPE and ISTC are mainly used to evaluate the performance of either PEC device or photoanode based on the photocurrent and photo-voltage. However, none of the above efficiencies provides the performance evaluation based on the total power output generated from PEC device which is based on the total current density obtained due to contribution from applied bias and light. Hence, in order to do so, we propose a new efficiency metric called "electrical and solar power-to-hydrogen (ESPH)" which is based on the definition of efficiency i.e. total power output divided by total power input.

We measured ESPH for hydrogenated N-S co-doped TiO_2@800ºC/24h electrode, which includes the external applied electrical power, along with solar power as total power input.

$$ESPH\ (based\ on\ collected\ H_2\ gas) = \left[\frac{(mmoles\ of\ H_2/s) \times (237\ kJ/mol)}{(V_b \times I_{dark} + P_{total})(mW/cm^2) \times Area(cm^2)}\right]_{AM\ 1.5G} \times 100 \quad \text{..... (5)}$$

$$ESPH\ (based\ on\ current) = \left[\frac{|j_{PEC}\ (mA/cm^2)| \times 1.23(V)}{(V_b \times I_{dark} + P_{total})(mW/cm^2) \times Area(cm^2)}\right]_{AM\ 1.5G} \times 100 \quad \text{..... (6)}$$

During water splitting reaction, oxygen and hydrogen gases were collected at working and counter electrodes respectively. Evolved gases were observed to be in stoichiometric ratio which suggests that there is no side product formation. The sample shows ESPH efficiency of ~ 1.18% and 7.2%at 0.63 and 1.56 V applied bias respectively which is highest ESPH efficiency among all other samples (Figure7d). The possible reasons for lower ESPH efficiency: (1) it is measured in two-electrode configuration and gives full cell efficiency and (2) it includes all the parasitic losses arise from different components of PEC cell. Figure 7c shows a plot of hydrogen collected during reaction vs. applied bias for the same sample under light illumination condition. Further, ESPH efficiencies (based on moles of H_2 production) under illumination (@ ~1.56 V bias) for this sample is ~ 5.83%. Additionally, we calculated

the amount of hydrogen generated based on current density as well as based on collection as shown in Figure 7c. The difference in ESPH as well as production of H_2 based on current and moles of hydrogen collection can be attributed to ohmic drop (IR drop) and other associated resistances during the collection of evolved gases using "inverted beaker method" (Figure S19).

3.3 Electrochemical Impedance Spectra (EIS) analysis

The electrode/electrolyte interface kinetics and dynamics of electron transport of fabricated nanostructures can be analyzed from EIS analysis[46, 47]. We performed EIS measurements to investigate the conductivity and impedance values for best sample "hydrogenated N-S co-doped TiO_2@800ºC/24h" on SS substrates under dark and light conditions (Figure S17); The experimental and simulated patterns matches with $R_S(R_1C)(R_2Q)$ circuit (inset image of Figure S17a), where R_S represents solution resistance of the electrolyte (i.e. ohmic resistance including the resistance of the electrolyte, separator and electrical contacts), C and Q being capacitance and constant phase element, R_1 and R_2 being the resistance associated in charge transfer process. The two semicircles correspond to oxide/hydroxide covered mixed surface[48]. The double layer charge capacitance (C_{dl}) vs. applied potential data of this sample is given in Table S6a. Further, decrease in charge transfer resistance upon illumination is observed from decrease in diameter of the semicircle as shown in Figure S17b, which signifies the enhancement in charge transport rate due to increase in photon absorption cross section. This is because the illuminated light source provides additional electrochemical potential which helps in overcoming the activation energy for electrochemical reaction. Further, EIS measurements were performed on three control samples (Anatase TiO_2, hydrogenated N-S co-doped TiO_2@800°C/24h and hydrogenated N-S co-doped TiO_2@800°C/72h) in faradaic zone (0.5 V, 0.6 V, 0.7 V, and 0.8 V vs. Ag/AgCl) under light conditions (Figure 8) to trace the charge transfer kinetics which is informative of the charge carrier recombination rate (films on fluorine doped tin oxide FTO substrate). Inset image in Figure 8(d) shows the equivalent circuit ($(R_s(R_f(R_{ct}C_\mu)C_{dl}))$) which is chosen for fitting the Nyquist data proposed by Bisqert et.al.[49, 50] for three control samples. The reason for choosing this circuit is, after illumination of light on photoanode, electron hole pair gets generated. Some of the excited electrons in the conduction band form the double layer

capacitance (C_{dl}) with ions in the electrolyte and rest of the electrons recombine with holes in the valance band (which is denoted as film resistance (R_f)). Since C_{dl} and R_f are mutually inclusive events, these two are kept in parallel. Further, the fraction of holes which are left after recombination with electrons are transported from the surface to species to oxidize them (R_{ct}, which is the measure of charge transport from the valence band of semiconductor to the electrolyte (i.e. less the charge transfer resistance, more the activity towards oxidation/reduction of the species)) and rest of the fraction forms the chemical capacitance (C_μ, which denotes the concentration of holes in the valence band). Since Rct and C_μ are inclusive events and series events with charge carrier recombination (R_f), R_{ct} and C_μ are in parallel and these are in series with R_f. After inclusion of solution resistance (R_s) in to the circuit, which is a series event with all of the above mentioned system, the overall EIS circuit is ($R_s(R_f(R_{ct}C_\mu)C_{dl})$).

From the fitted data of the EIS circuits, we infer that there is a decrease in the resistance of film (which is measure of charge carrier recombination) for hydrogenated N-S co-doped TiO_2@800ºC/24h sample over anatase TiO_2 and hydrogenated N-S co-doped TiO_2@800ºC/72h samples at 0.5, 0.6, 0.7 and 0.8 V potentials (Figure 8 and Table S6b). This result confirms the hydrogenated N-S co-doped TiO_2@800ºC/24h sample having faster charge carrier separation in comparison to other two samples[51]. Therefore, improvement in optical absorption does not lead to enhance the photo performance as charge carrier recombination step is dominating. It is to be noted that the measure of double layer capacitance is an indicative of the active surface available for electrochemical reaction (ECSA) if the specific capacitance, C_s (capacitance of an atomically smooth planar surface per unit area) of the material under identical electrolytic conditions is known[52]. Therefore, the double layer capacitance (C_{dl}) calculated from EIS circuits (Table S6b) represents the electrochemical surface area (ECSA) available for electrochemical reaction. From Table S6b, it can be concluded that 24 h hydrogenated sample possess better ECSA than 72 h hydrogenated sample. Additionally, the low charge transfer resistance, R_{ct} (which is measure of faradaic activity at electrode/electrolyte interface) of 24 h hydrogenated sample also reflects the same. Therefore, surface electrochemistry parameter cannot be ruled out in true activity measurement of electrodes used in PEC water splitting reaction. This experimental data assists in inferring the interplay of

the coupled parameters (optical absorption, charge carrier separation, and surface electrochemistry) in enhancing the PEC water splitting reaction.

3.4 Role of amorphous layer/surface disorder

Sputtering via focused ion beam (FIB) was employed to remove few atomic layers from surface disordered/hydrogenated TiO_2. For this purpose, we have taken N doped TiO_2@500°C/24h sample for study. SEM images of FIB sputtered sample show smoother surface (Figure 9b) in comparison to unsputtered sample (Figure 9d). The UV-Vis spectrum of sputtered sample (Figure 9c) shows a blue shift in absorption with respect to unsputtered sample. This confirms that defects contributing to lowering of band gap and they are concentrated in the first few surface and subsurface layers in comparison to bulk. From Raman spectra, a decrease in peak intensity ratio (B_{1g}/E_g or D/G) is observed for sputtered portion of the sample over unsputtered portion (Figure S18a and S18b). This observation further confirms removal of surface defects present on disordered/amorphous surface upon FIB sputtering. Further, the XPS spectra peaks of sputtered and un-sputtered portions (Figure S12d) of the sample were tabulated in Table S7. There is no noticeable change from FTIR and XRD analysis before and after FIB sputtering (Figure S18c and S18d).

The sputtered sample shows less EC activity in comparison to unsputtered sample (Figure 10a). Further, the change in surface structure of the sample upon sputtering is observed from additional redox peaks in non-faradiac region of CV (Figure 10b). In addition, decrease in PEC performance is observed for sputtered sample over unsputtered part (Figure 10c). The calculated ABPE efficiency for sputtered and unsputtered portions of the sample is ~ 0.06, and 0.1% respectively (Figure 10d). Further, reduction in differential capacitance value (at 0.1 V and 0.2 V) is observed after sputtering/removing few atomic layers from the sample (Table S8) which suggests reduction in electrocatalytic active sites. The surface disorder/amorphous layer is found to be beneficial for enhancement of electrocatalytic activity, photon absorption cross-section and charge carrier transport which is in agreement with recent literature reports[53, 54].

4. Conclusions

In the present work, we explore the issue of enhancement in optical absorption cross section and EC activity without compromising electron-hole pair separation in PEC water splitting reaction via hydrogenated (N-S) doped TiO_2 nanostructures. The maximum EC/PEC activity is found in hydrogenated N-S co-doped TiO_2@800ºC/24h sample with an applied bias photon to current conversion efficiency (ABPE) of ~ 0.38% @0.628 V applied bias, intrinsic solar to chemical conversion efficiency (ISTC) of ~ 3.1% @1.27 V (vs. RHE) and electrical and solar power-to-hydrogen (ESPH) conversion efficiency of ~ 6.6%@1.56 V applied bias. The enhancement in PEC performance in the co-doped hydrogenated TiO_2 samples over doped/unhydrogenated TiO_2 samples is attributed to the combined effect of dopants, oxygen vacancy states and Ti^{3+} states. The photon absorption cross-section is increased by shifting VB upward through introduction of less electronegative dopants (N, S) and lowering of CB through formation of Ti^{3+} upon hydrogenation. The presence of Ti^{3+} state and oxygen vacancies are confirmed through Raman, EPR, and XPS studies. Further, double layer capacitance (C_{dl}), charge transfer resistance (R_{ct}), and film resistance (R_f) data obtained from electrochemical impedance spectroscopy (EIS) analysis also supports the view point that optical absorption, charge carrier separation, and surface electrochemistry are not mutually exclusive path ways in enhancing the PEC performance of surface disordered/hydrogenated TiO_2.The formation of Ti^{3+} state and oxygen vacancies due to hydrogenation lead to a few layers of disordered surface/subsurface region. Removal of surface layers through focused ion beam sputtering result in blue-shift of absorption spectrum and also in decrease of both electrochemical (EC) and photoelectrochemical (PEC) activity. This signifies that the surface disordered layer plays a vital role in both enhancing electrocatalytic activity as well as enhancing photon absorption. However, increase in defect states (Ti^{3+} and oxygen vacancy) beyond a point (extending towards bulk), while increasing the photon absorption cross section, reduces the charge-carrier separation/transport and EC activity which in turn reduce the PEC activity. The understanding from the present work helps in partial decoupling the effects of photon absorption cross-section, surface electrochemistry, charge-carrier transport and paves the way for rational material design for water oxidation PEC catalyst.

Acknowledgement

We gratefully acknowledge the support from the Technology System Development program of the Department of Science and Technology (DST), Government of India *via* project DST/TSG/SH/2011/106.

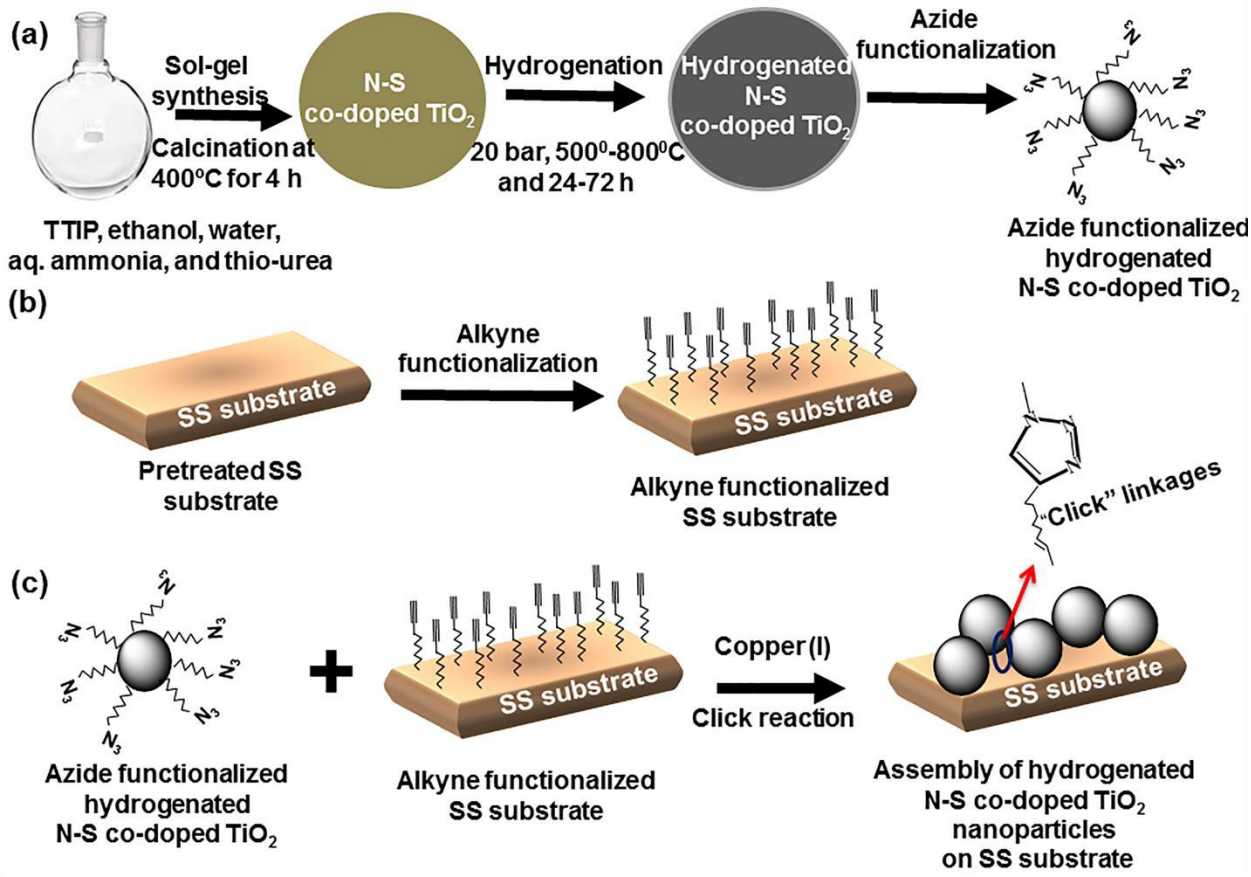

Scheme 1 Schematic representation of synthesis and fabrication hydrogenated N-S co-doped TiO_2 nanostructures onto alkyne functionalized stainless steel (SS) substrate via click chemistry.

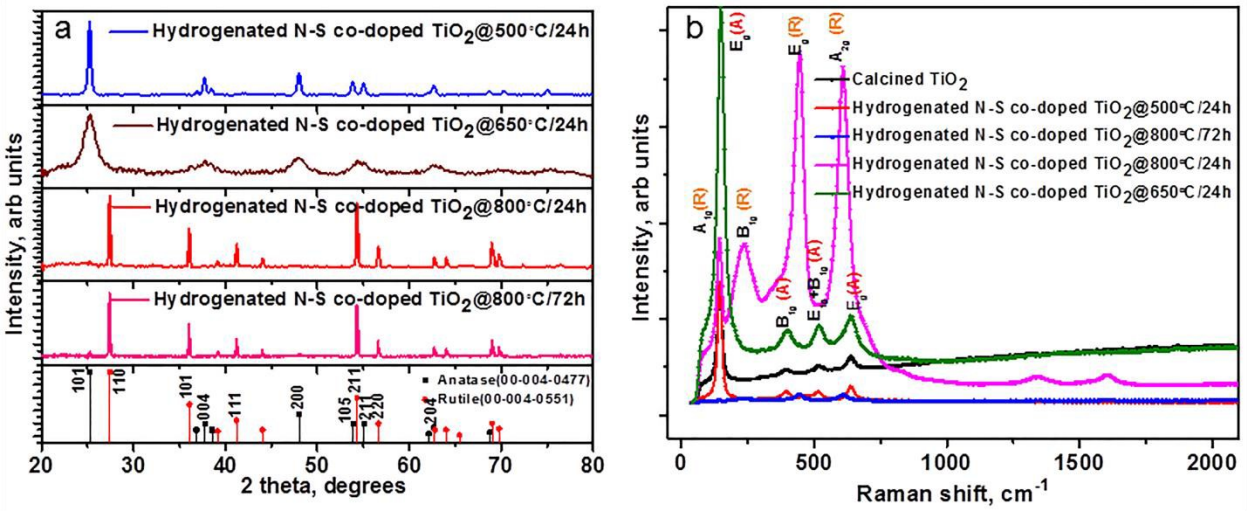

Fig. 1 (a) XRD; and (b) Raman spectra of undoped TiO_2 and hydrogenated N-S co-doped TiO_2 samples.

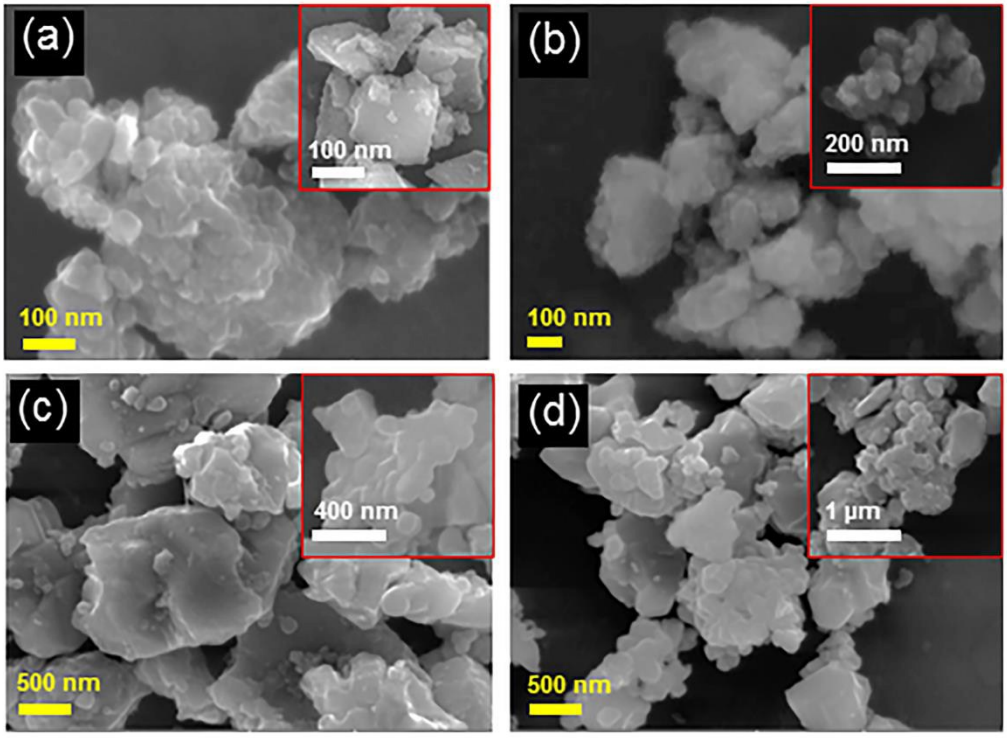

Fig. 2 SEM images of (a) hydrogenated N-S co-doped TiO_2@500ºC/24h; (b) hydrogenated N-S co-doped TiO_2@650ºC/24h; (c) hydrogenated N-S co-doped TiO_2@800ºC/24h; and (d) hydrogenated N-S co-doped TiO_2@800ºC/72h.

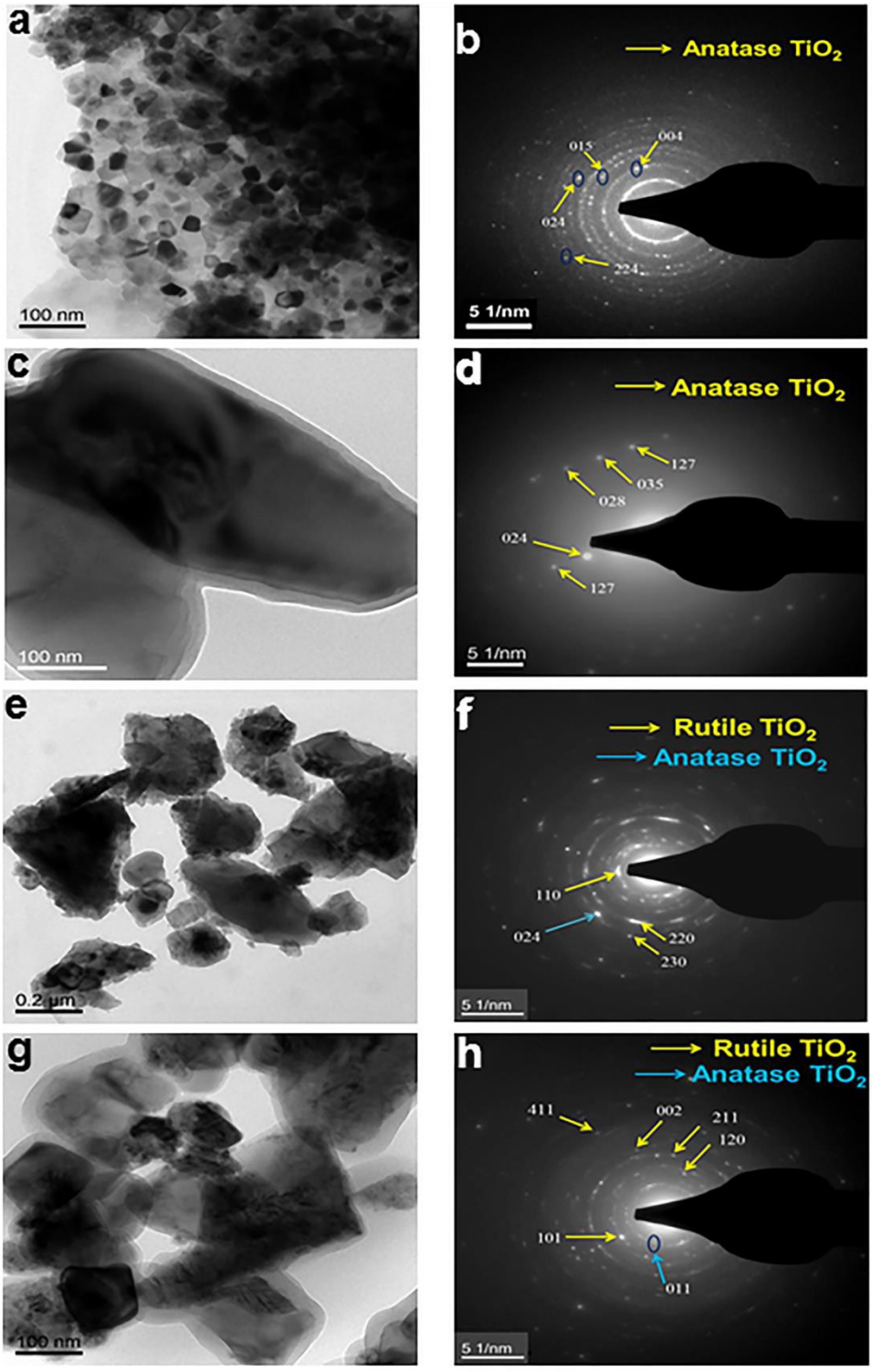

Fig. 3 TEM images of N-S co-doped TiO_2 hydrogenated at temperature of (a) 500 °C; (c) 650 °C; (e) 800 °C for 24 h; and (g) 800 °C for 72 h; and b, d, f and h are corresponding SAED patterns.

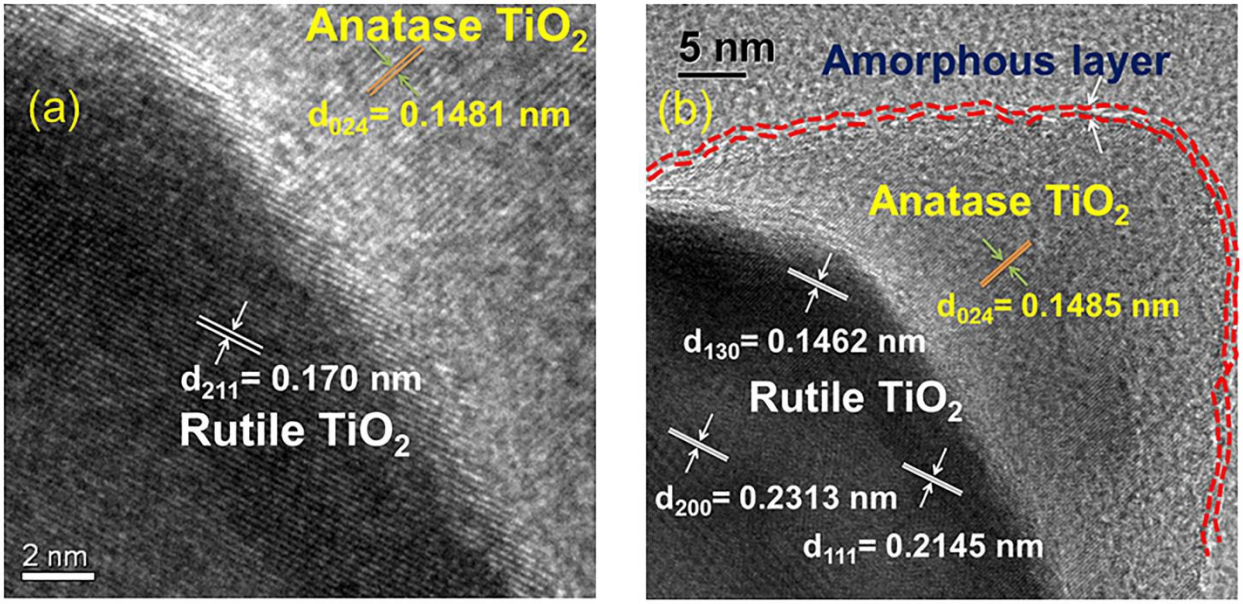

Fig. 4 HRTEM image of hydrogenated N doped TiO_2@700ºC/24h sample showing (a) anatase-rutile phase interfaces; and (b) amorphous layer over crystalline core.

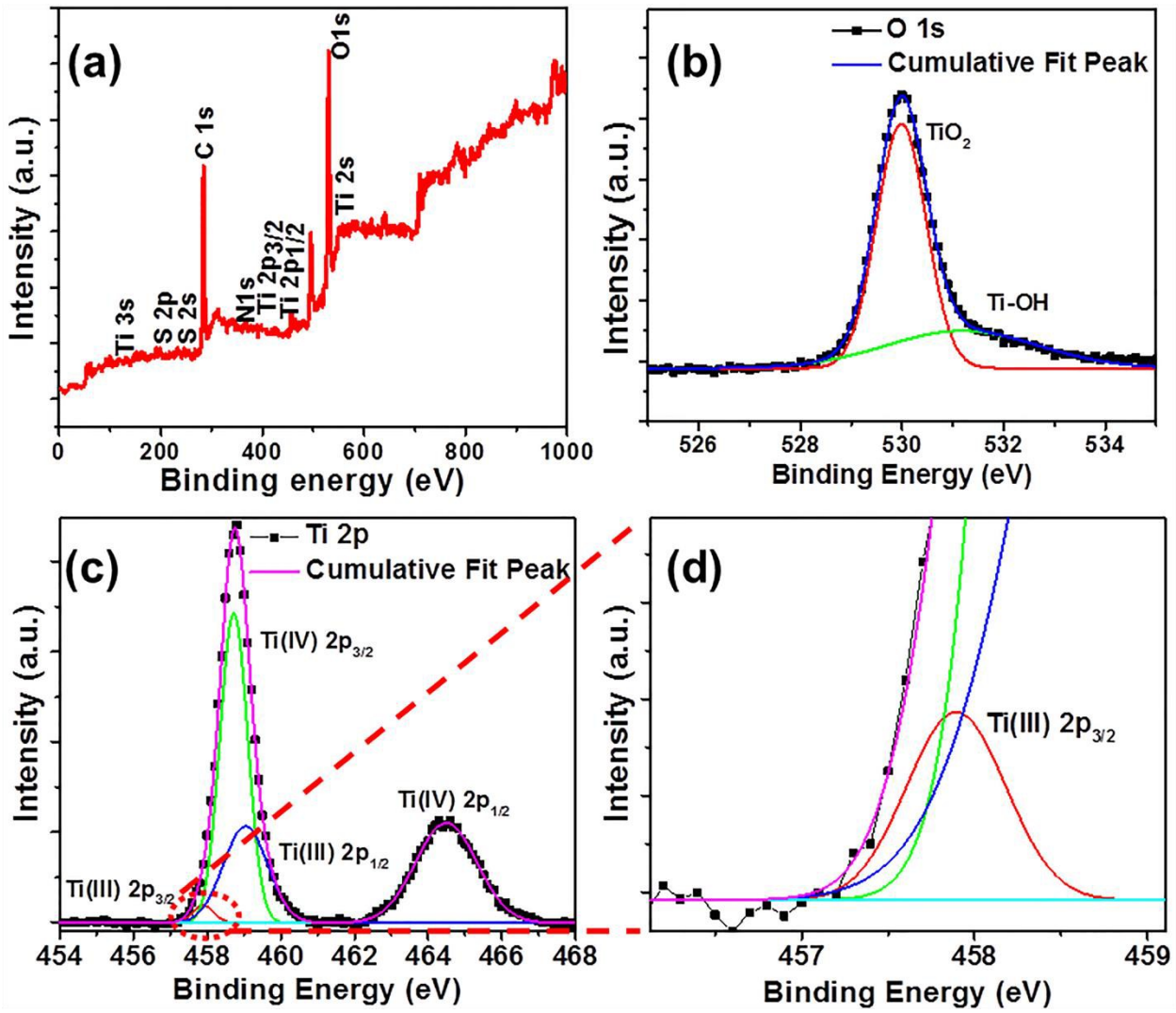

Fig. 5 XPS spectra of hydrogenated N-S co-doped TiO_2@800°C/24h: a) whole scan, b) O 1s, c) Ti 2p, and d) enlarged/resolved portion (red dotted lines of c) of Ti 2p XPS peak.

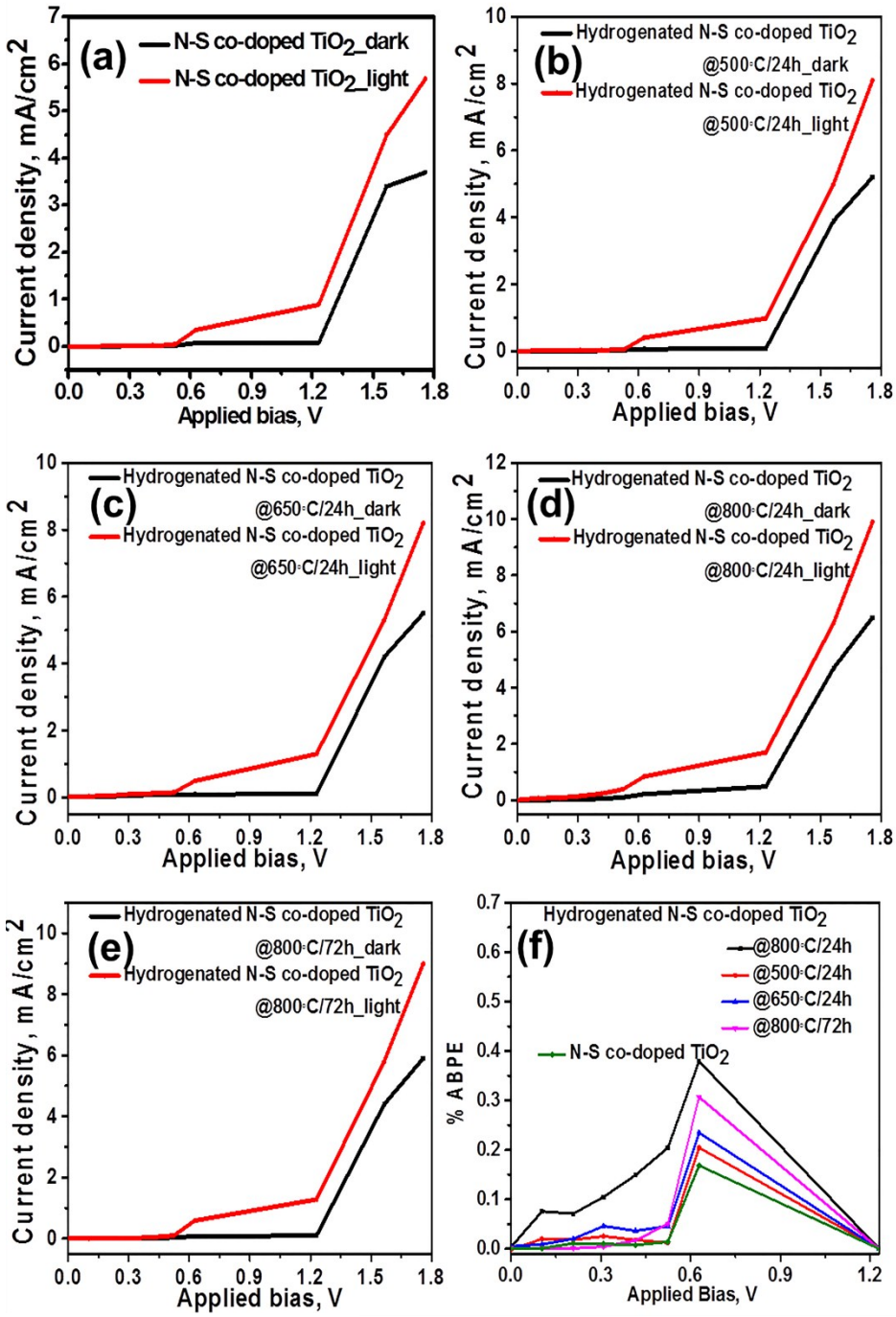

Fig. 6 Current vs. applied bias plots of (a) N-S co-doped TiO_2; (b) hydrogenated N-S co-doped TiO_2@500ºC/24h; (c) hydrogenated N-S co-doped TiO_2@650ºC/24h; (d) hydrogenated N-S co-doped TiO_2@800ºC/24h; (e) hydrogenated N-S co-doped TiO_2@800ºC/72h, and (f) Applied bias to photo-conversion efficiency (ABPE) of all N-S co-doped hydrogenated TiO_2 samples performed in 0.1M NaOH solution (two-probe measurements).

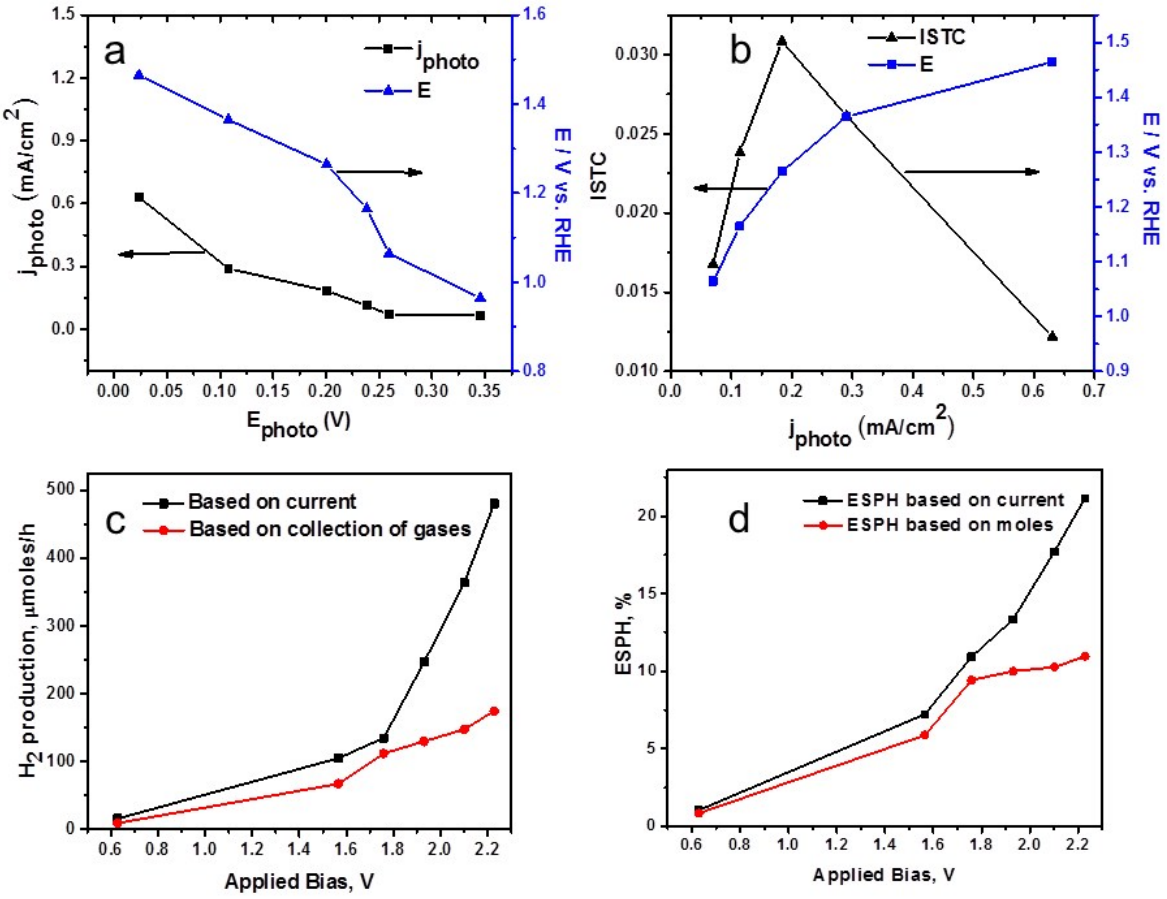

Fig. 7 (a) Intrinsic photovoltaic power characteristics; (b) Intrinsic solar to chemical conversion (ISTC) efficiency; (c) micromoles of hydrogen production; and (d) electrical and solar power-to-hydrogen (ESPH) conversion efficiency based on current and moles of hydrogen collected for hydrogenated N-S co-doped TiO_2@800ºC/24h sample.

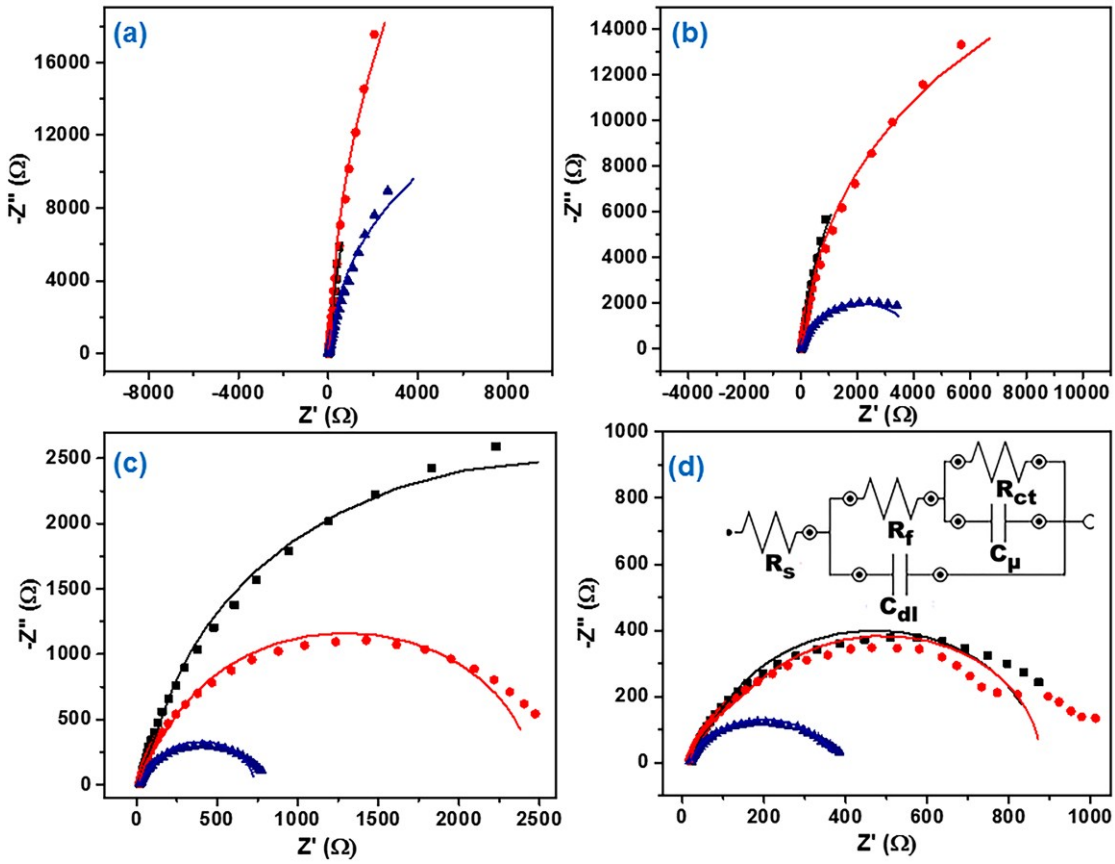

Fig. 8 Electrochemical Impedance Spectroscopy (EIS) of anatase TiO_2 (black square), hydrogenated N-S co-doped TiO_2@800°C/24h (blue triangle) and hydrogenated N-S co-doped TiO_2@800°C/72h (red circle) under light condition at different potentials (vs. Ag/AgCl) (a) 0.5 V, (b) 0.6 V, (c) 0.7 V, and (d) 0.8 V (symbols represent the experimental data, lines represent the fitted data, and inset in figure **d** represents the EIS circuit).

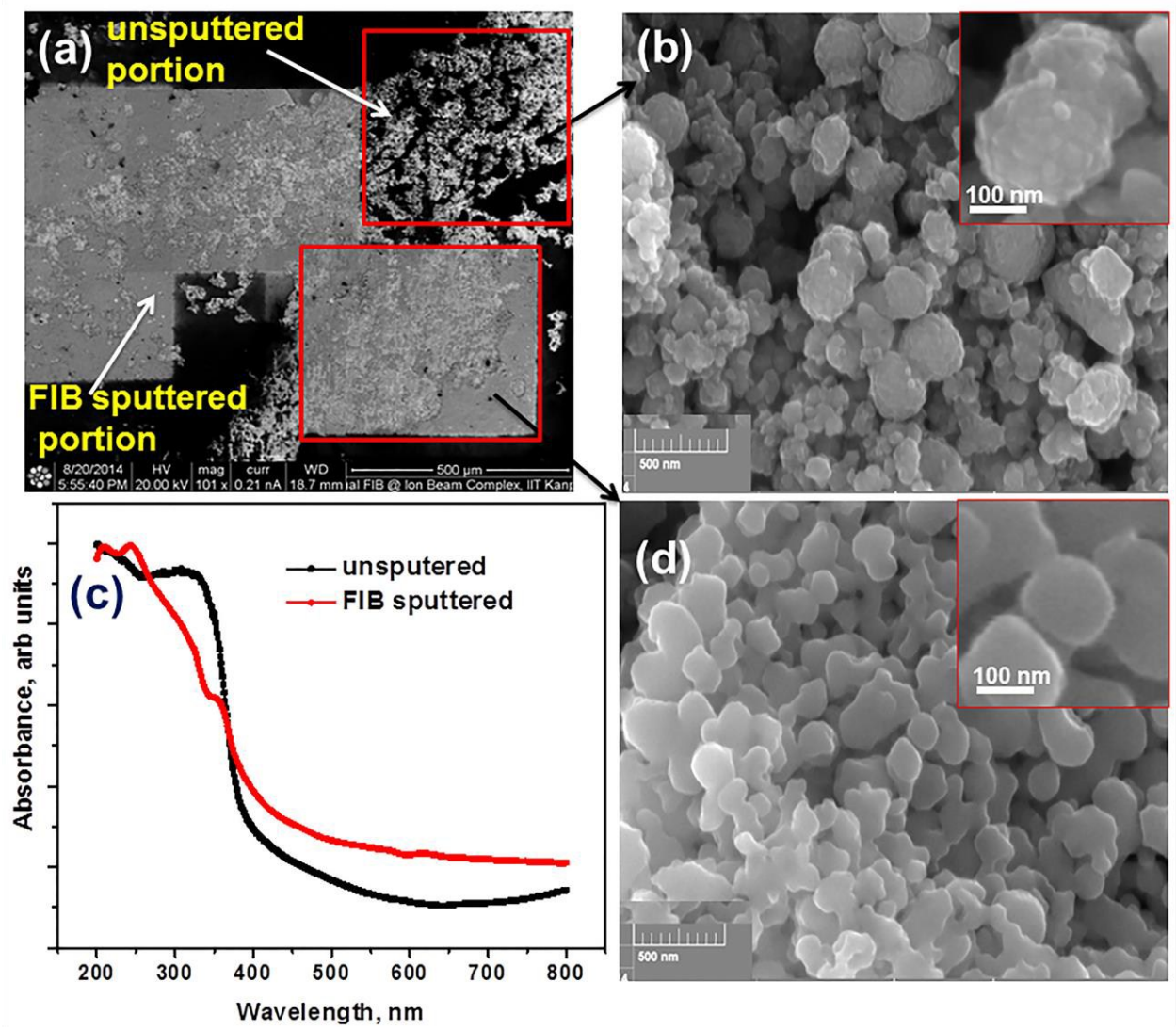

Fig. 9 SEM images of hydrogenated N doped TiO_2@500ºC/24h: (a) at normal resolution, (b) unsputtered portion, (d) FIB sputtered portion; and (c) UV-Vis spectra of FIB sputtered and unsputtered portion of the sample hydrogenated N doped TiO_2@500ºC/24h.

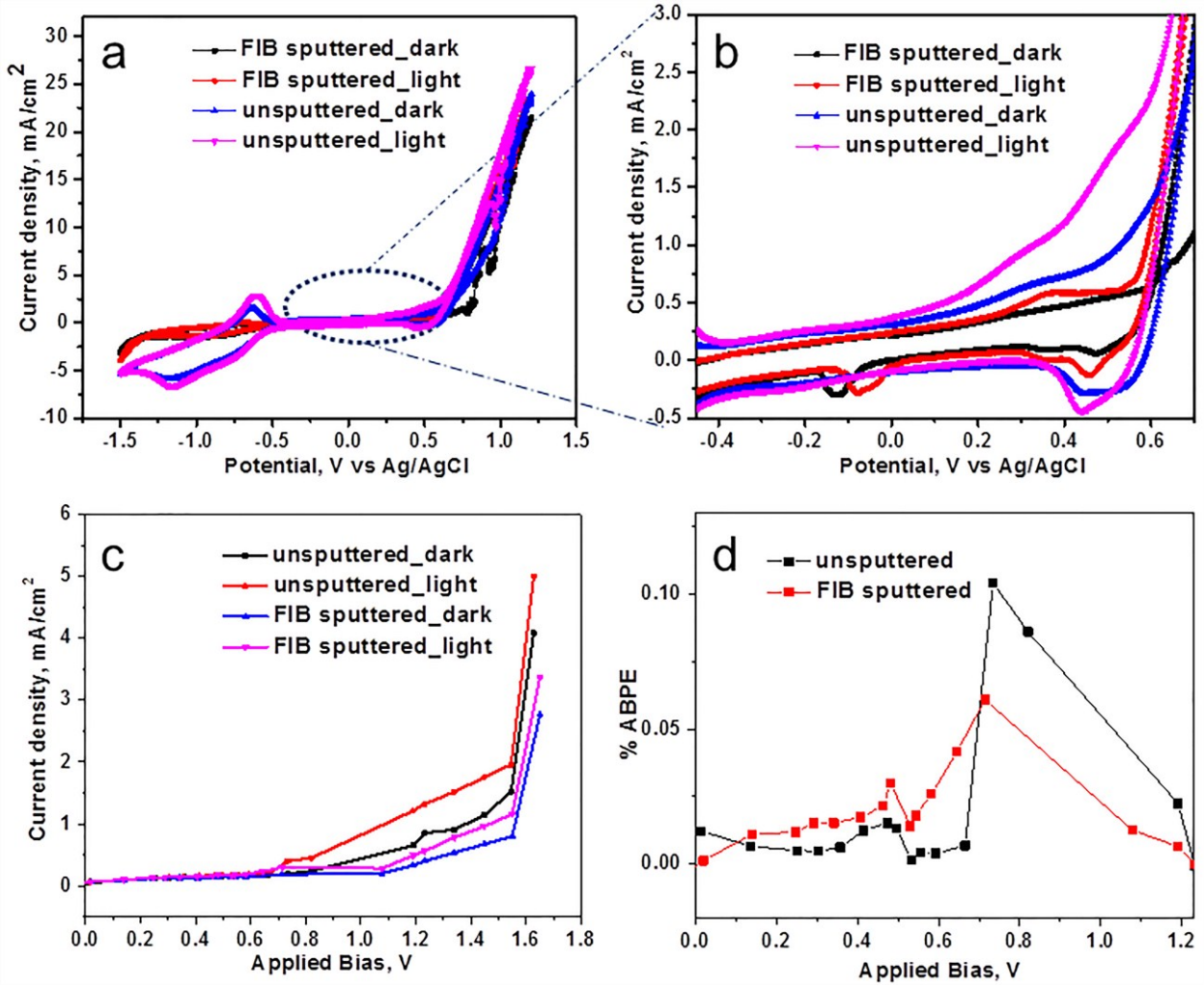

Fig. 10 EC/PEC data of hydrogenated N doped TiO_2@500ºC/24h sample before and after FIB sputtering: a) cyclic voltammetry data (3-probe), b) enlarged portion of fig **a**, c) current vs. applied bias plots (2-probe); and d) % applied bias photon to current conversion efficiency (ABPE).

References

1. X. B. Chen, L. Liu, P. Y. Yu and S. S. Mao, *Science*, 2011, **331**, 746-750.
2. A. Naldoni, M. Allieta, S. Santangelo, M. Marelli, F. Fabbri, S. Cappelli, C. L. Bianchi, R. Psaro and V. Dal Santo, *Journal of the American Chemical Society*, 2012, **134**, 7600-7603.
3. N. Roy, Y. Sohn, K. T. Leung and D. Pradhan, *J. Phys. Chem. C*, 2014, **118**, 29499-29506.
4. T. Lin, C. Yang, Z. Wang, H. Yin, X. Lu, F. Huang, J. Lin, X. Xie and M. Jiang, *Energy & Environmental Science*, 2013, **7**, 967-972.
5. D. M. Jang, I. H. Kwak, E. L. Kwon, C. S. Jung, H. S. Im, K. Park and J. Park, *J. Phys. Chem. C*, 2015.
6. Q. Xiang, J. Yu, W. Wang and M. Jaroniec, *Chem. Comm.*, 2011, **47**, 6906-6908.
7. R. Su, R. Bechstein, J. Kibsgaard, R. T. Vang and F. Besenbacher, *J. Mater. Chem.*, 2012, **22**, 23755-23758.
8. L. Cai, I. S. Cho, M. Logar, A. Mehta, J. He, C. H. Lee, P. M. Rao, Y. Feng, J. Wilcox, F. B. Prinz and X. Zheng, *Phys. Chem. Chem. Phys.*, 2014, **16**, 12299-12306.
9. J. Buha, *Journal of Physics D: Applied Physics*, 2012, **45**, 385305.
10. W. D. Chemelewski, H.-C. Lee, J.-F. Lin, A. J. Bard and C. B. Mullins, *J. Am. Chem. Soc.*, 2014, **136**, 2843-2850.
11. R. D. L. Smith, M. S. PreÌ • vot, R. D. Fagan, S. Trudel and C. P. Berlinguette, *J. Am. Chem. Soc.*, 2013, **135**, 11580-11586.
12. R. D. L. Smith, B. Sporinova, R. D. Fagan, S. Trudel and C. P. Berlinguette, *Chem. Mater.*, 2014, **26**, 1654-1659.
13. E. Fabbri, A. Habereder, K. Waltar, R. Kotz and T. J. Schmidt, *Catal. Sci. Tech.*, 2014, **4**, 3800-3821.
14. S. Hoang, S. P. Berglund, N. T. Hahn, A. J. Bard and C. B. Mullins, *Journal of the American Chemical Society*, 2012, **134**, 3659-3662.
15. L. Mi, Y. Zhang and P.-N. Wang, *Chemical Physics Letters*, 2008, **458**, 341-345.
16. S. P. Russo, I. E. Grey and N. C. Wilson, *The Journal of Physical Chemistry C*, 2008, **112**, 7653-7664.
17. O. Diwald, T. L. Thompson, T. Zubkov, E. G. Goralski, S. D. Walck and J. T. Yates, *The Journal of Physical Chemistry B*, 2004, **108**, 6004-6008.
18. R. W. Shunhang Wei, Jikang Jian, Fengjuan Chen and Yanfei Sun, *Dalton Trans.*,, 2015, **44**, 1534–1538.
19. X. Yang, C. Cao, L. Erickson, K. Hohn, R. Maghirang and K. Klabunde, *Applied Catalysis B: Environmental*, 2009, **91**, 657-662.
20. H. Liu and L. Gao, *Journal of the American Ceramic Society*, 2004, **87**, 1582-1584.
21. X. Pan, M.-Q. Yang, X. Fu, N. Zhang and Y.-J. Xu, *Nanoscale*, 2013, **5**, 3601-3614.
22. Z. Wang, C. Yang, T. Lin, H. Yin, P. Chen, D. Wan, F. Xu, F. Huang, J. Lin and X. Xie, *Advanced Functional Materials*, 2013, **23**, 5444-5450.
23. A. P. Upadhyay, D. K. Behara, G. P. Sharma, A. Bajpai, N. Sharac, R. Ragan, R. G. S. Pala and S. Sivakumar, *Acs Applied Materials & Interfaces*, 2013, **5**, 9554-9562.
24. J. Lynch, C. Giannini, J. K. Cooper, A. Loiudice, I. D. Sharp and R. Buonsanti, *J. Phys. Chem. C*, 2015, **119**, 7443-7452.
25. C. L. Haynes and R. P. Van Duyne, *The Journal of Physical Chemistry B*, 2001, **105**, 5599-5611.

26. J. M. Coronado, A. J. Maira, J. C. Conesa, K. L. Yeung, V. Augugliaro and J. Soria, *Langmuir*, 2001, **17**, 5368-5374.
27. H. Liu, H. T. Ma, X. Z. Li, W. Z. Li, M. Wu and X. H. Bao, *Chemosphere*, 2003, **50**, 39-46.
28. N. Serpone, *The Journal of Physical Chemistry B*, 2006, **110**, 24287-24293.
29. T. Berger, M. Sterrer, O. Diwald, E. Knözinger, D. Panayotov, T. L. Thompson and J. T. Yates, *The Journal of Physical Chemistry B*, 2005, **109**, 6061-6068.
30. A. Fujishima, T. N. Rao and D. A. Tryk, *Journal of Photochemistry and Photobiology C: Photochemistry Reviews*, 2000, **1**, 1-21.
31. T. Su, Y. Yang, Y. Na, R. Fan, L. Li, L. Wei, B. Yang and W. Cao, *ACS applied materials & interfaces*, 2015, **7**, 3754-3763.
32. J. Cai, K. Lv, J. Sun and K. Deng, *RSC Adv.*, 2014, **4**, 19588-19593.
33. L. Xiong, M. Ouyang, L. Yan, J. Li, M. Qiu and Y. Yu, *Chemistry Letters*, 2009, **38**, 1154-1155.
34. X. Lu, G. Wang, T. Zhai, M. Yu, J. Gan, Y. Tong and Y. Li, *Nano letters*, 2012, **12**, 1690-1696.
35. J. M. Buriak, P. V. Kamat and K. S. Schanze, *Acs Applied Materials & Interfaces*, 2014, **6**, 11815-11816.
36. C. H. Choi, S. H. Park and S. I. Woo, *ACS nano*, 2012, **6**, 7084-7091.
37. P. Chen, T.-Y. Xiao, H.-H. Li, J.-J. Yang, Z. Wang, H.-B. Yao and S.-H. Yu, *ACS nano*, 2012, **6**, 712-719.
38. E. L. Miller and R. E. Rocheleau, *Journal of the Electrochemical Society*, 1997, **144**, 3072-3077.
39. H. Zhang, X. Lv, Y. Li, Y. Wang and J. Li, *ACS nano*, 2009, **4**, 380-386.
40. D. C. Hurum, A. G. Agrios, K. A. Gray, T. Rajh and M. C. Thurnauer, *The Journal of Physical Chemistry B*, 2003, **107**, 4545-4549.
41. A. Sclafani and J. M. Herrmann, *The Journal of Physical Chemistry*, 1996, **100**, 13655-13661.
42. C. Yang, Z. Wang, T. Lin, H. Yin, X. Lü, D. Wan, T. Xu, C. Zheng, J. Lin and F. Huang, *Journal of the American Chemical Society*, 2013, **135**, 17831-17838.
43. G. Wang, H. Wang, Y. Ling, Y. Tang, X. Yang, R. C. Fitzmorris, C. Wang, J. Z. Zhang and Y. Li, *Nano letters*, 2011, **11**, 3026-3033.
44. H. Cui, W. Zhao, C. Yang, H. Yin, T. Lin, Y. Shan, Y. Xie, H. Gu and F. Huang, *J. Mater. Chem. A*, 2014, **2**, 8612-8616.
45. Y. Yao, G. Li, S. Ciston, R. M. Lueptow and K. A. Gray, *Environmental science & technology*, 2008, **42**, 4952-4957.
46. B. Klahr, S. Gimenez, F. Fabregat-Santiago, J. Bisquert and T. W. Hamann, *Energy & Environmental Science*, 2012, **5**, 7626-7636.
47. P. L. V. Luca Gael Bertoluzzi, Juan Antonio Jimenez Tejada and Juan Bisquert *J. Mater. Chem A*, 2015.
48. Y.-H. Fang and Z.-P. Liu, *J. Am. Chem. Soc.*, 2010, **132**, 18214-18222.
49. L. Bertoluzzi and J. Bisquert, *J. Phys. Chem. Lett.*, 2012, **3**, 2517-2522.
50. L. Bertoluzzi, P. Lopez-Varo, J. A. J. Tejada and J. Bisquert, *J. Mater. Chem. A*, 2016.
51. T. Lopes, L. Andrade, F. Le Formal, M. Gratzel, K. Sivula and A. Mendes, *Physical Chemistry Chemical Physics*, 2014, **16**, 16515-16523.

52. C. C. McCrory, S. Jung, J. C. Peters and T. F. Jaramillo, *Journal of the American Chemical Society*, 2013, **135**, 16977-16987.
53. P. Yan, G. Liu, C. Ding, H. Han, J. Shi, Y. Gan and C. Li, *Acs Applied Materials & Interfaces*, 2015, **7**, 3791-3796.
54. T. Xia, W. Zhang, W. Li, N. A. Oyler, G. Liu and X. Chen, *Nano Energy*, 2013, **2**, 826-835.

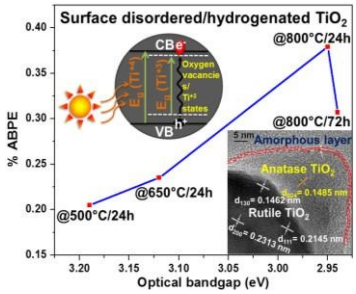

TOC Graphic: Coupled optical absorption, charge carrier separation, and surface electrochemistry in surface disordered/hydrogenated TiO_2 for enhanced PEC water splitting reaction.